Featured in Physics

Microstructural Origin of Propagating Compaction Patterns in Porous Media

Lars Blatny and Paul Berclaz
School of Architecture, Civil and Environmental Engineering, Swiss Federal Institute of Technology, Lausanne (EPFL), CH-1015 Lausanne, Switzerland

François Guillard and Itai Einav
School of Civil Engineering, The University of Sydney, New South Wales, 2006, Australia

Johan Gaume*
School of Architecture, Civil and Environmental Engineering, Swiss Federal Institute of Technology, Lausanne (EPFL), CH-1015 Lausanne, Switzerland and WSL Institute for Snow and Avalanche Research SLF, CH-7260 Davos Dorf, Switzerland

(Received 27 July 2021; revised 16 February 2022; accepted 19 April 2022; published 1 June 2022)

Porous rocks, foams, cereals, and snow display a diverse set of common compaction patterns, including propagating or stationary bands. Although this commonality across distinct media has been widely noted, the patterns' origin remains debated—current models employ empirical laws for material-specific processes. Here, using a generic model of inelastic structured porous geometries, we show that the previously observed patterns can be attributed to a universal process of pore collapse. Furthermore, the pattern diversity can be mapped in a phase space of only two dimensionless numbers describing material strength and loading rate.

DOI: 10.1103/PhysRevLett.128.228002

Compaction processes in porous media are crucial to understanding avalanche release processes [1,2], earthquakes [3], biological and structural failures [4,5], permeability reduction in petroleum extraction [6], and heterogeneities forming in industrial powder packing [7]. During compression of corresponding media such as snow, sandstones, bones and foams, granular packs, and ceramics, various irreversible deformation patterns can be observed, including diffused compaction and localized "compaction bands" [8–13]. These bands may be either stationary or dynamic, where the localized deformed zone propagates spatially throughout the material. In confined compression experiments, propagating compaction bands have been found to screen through rocks only once [14], while in cereal packs [15,16] and snow [17], they frequently reflect from boundaries, crossing material points in oscillatory fashion.

While different patterns can be found within the same material under various experimental conditions, similar patterns can be observed across a wide span of other materials. This raises a question on the origin of such common compaction patterns. Put differently, what is the single unique physical trigger to the emergence of the universally observed compaction patterns within rocks, cereal packs, and snow? This question remains unanswered as most previous research focused on describing arrays of material-specific processes that are not common to all the aforementioned materials. Some continuum models introduced empirical laws to describe additional strain softening and time-dependent hardening of the material yielding [17]. Alternatively, other heuristic lattice-spring models were proposed to capture these dynamics [16], without imposing any rate- or time-dependent hardening, yet involving instead an empirical law for repetitive crushing of springs. In the following, we provide evidence supporting that the origin of the diverse compaction dynamics is linked to the physical microstructure of pores, without needing to employ empirical hardening, softening, or repetitive crushing.

To this aim, we simulate uniaxially confined compression of structured porous media using the material point method (MPM) [18]. Similar to the finite element method, MPM solves the weak form discretization of the mass and momentum conservation equations. The solid phase of the structures is discretized into a finite number of particles (material points) with constant mass and an associated deformation gradient. No meshing of the material domain is needed; however, a fixed background grid combined with particle-grid interpolation facilitates spatial differentiation. As MPM does not suffer from the mesh distortion issues typically associated with the classical finite element

method, this hybrid Eulerian-Lagrangian numerical scheme is particularly suitable for continuum modeling of solids under large deformations and with changes in topology [19,20]. Further details are presented in the Supplemental Material [21].

The continuous solid phase of the media is simulated as an elastoplastic material in the "simplest" possible way, using a Saint Venant-Kirchhoff elastic and von Mises perfectly plastic solid with a Young's modulus E, Poisson's ratio ν, and yield strength q_y such that $\sqrt{\frac{3}{2}\boldsymbol{s}:\boldsymbol{s}} \leq q_y$, where $\boldsymbol{s} = \boldsymbol{\tau} - (1/d)\mathrm{tr}(\boldsymbol{\tau})\boldsymbol{I}$ denotes the deviatoric part of the Kirchhoff stress tensor $\boldsymbol{\tau}$, and d the number of dimensions. Defining the deformed and undeformed coordinates $\boldsymbol{x}$ and $\boldsymbol{X}$, respectively, we make use of the common elastoplastic assumption of decomposing the deformation gradient tensor $\boldsymbol{F} = \partial\boldsymbol{x}/\partial\boldsymbol{X}$ into an elastic and a plastic part as $\boldsymbol{F} = \boldsymbol{F}^E\boldsymbol{F}^P$. The frame-indifferent, isotropic, and hyperelastic Saint Venant-Kirchhoff model relates the stress to the (elastic part of the) strain $\boldsymbol{\varepsilon}^E$ by

$$\boldsymbol{\tau} = \lambda \mathrm{tr}(\boldsymbol{\varepsilon}^E)\boldsymbol{I} + 2\mu\boldsymbol{\varepsilon}^E, \tag{1}$$

where $\lambda = \{E\nu/[(1+\nu)(1-2\nu)]\}$ and $\mu = \{E/[2(1+\nu)]\}$ are the Lamé parameters. Moreover, the Hencky strain tensor is given by

$$\boldsymbol{\varepsilon}^E = \frac{1}{2}\sum_{i=1}^{d} \log\lambda_i^2 \boldsymbol{n}_i \otimes \boldsymbol{n}_i, \tag{2}$$

where λ_i are the principal stretches whose squares are the eigenvalues of the left Cauchy-Green deformation tensor $\boldsymbol{b}^E = \boldsymbol{F}^E(\boldsymbol{F}^E)^T$ with corresponding eigenvectors $\boldsymbol{n}_i$.

We start by considering two-dimensional rectangular structures perforated with 578 regularly spaced square holes of the same size. Initially, these structures have a height h_0, side length $h_0/2$, and solid area fraction ϕ. They are subjected to confined uniaxial compression with a top plate moving down at a constant speed V and zero-friction slipping boundary conditions. Poisson's ratio $\nu = 0.3$, density $\rho = 1000\ \mathrm{kg/m^2}$, and yield strength $q_y = 250\ \mathrm{N/m}$ of the solid matrix are kept fixed in the simulations. In the absence of gravity, the parameter h_0 is arbitrary as it only results in a scaling of time.

With this simple model setup, Fig. 1 reveals different dynamic compaction patterns depending on the material and loading parameters. Specifically, we identify six classes of patterns: (a) nonreflecting compaction band, (b) reflecting band, (c) crossing bands emerging from the two ends of the structure, (d) erratic failure scattered randomly throughout the structure, (e) an explosive compaction zone creating a boundary between deformed and undeformed regions, or (f) buckling of the structural elements typically causing one or more growing compaction zones. These distinct compaction patterns have been observed experimentally in various materials. In particular, class (a) has been seen in steel foams [22] and sandstone [23,24], (b)–(d) in puffed rice [16], (b),(d) also in snow [17], (e) in porous aluminum powder samples [25], and (f) in polycarbonate foams [5].

Furthermore, we find that the patterns can be fully mapped using only two dimensionless parameters:

$$S \equiv \frac{V}{\sqrt{E/\rho}}, \qquad R \equiv \frac{q_y}{E}, \tag{3}$$

where S is a Mach number comparing the loading speed to the elastic wave speed in the solid matrix of the samples, while R compares the yield strength to the elastic modulus of the solid matrix. In the phase space defined by S and R, we categorize the observations into the six classes displayed in Figs. 1(a)–(f). This is presented in Fig. 2. In addition, we color the regions in this phase space according to the deformation mechanism on the microscale. It has been validated that as long as S and R are kept constant, the observed patterns do not change for any arbitrary value of the yield strength q_y, density ρ, and Poisson's ratio ν of the solid matrix. However, in transitional regions between different classes, we may observe deformation attributes of more than one class, and the classification of an experiment is therefore associated with some degree of subjectivity. While the onset of class (f) is porosity-dependent, as discussed later, the pattern classification generally holds for solid area fractions ϕ between approximately 0.25 and 0.75.

On the microstructural level, an unreflected band or a band with only one reflection is a result of diffuse failure of the constituent solid column elements as they expand and fill the surrounding pore spaces upon compression. In the case of a nonreflecting band, the pore spaces in the first row are completely filled before the compaction progresses to the next row of column elements. This process continues until all pore spaces are filled, at which point the structure is completely dense and the band has reached the end of the structure. For bands making one or more reflections, pore spaces in one row are only partially filled before the plastic deformations advance to the next row of columns. In order to reach a dense state, the compaction band must reflect and return to fill the remaining pore spaces, often with multiple reflections needed to accomplish this. In cases with two or more band reflections, the columns do not expand in a diffusive manner. Instead, we observe the occurrence of shear bands in the column elements, oriented at $\pm 45°$ as expected in a von Mises material obeying an associated flow rule. This causes these columns to bulge out laterally, effectively thickening the columns as the model permits no plastic volume change within the solid itself. The deformation then progresses to the next row of elements rather than immediately filling the current row of voids by

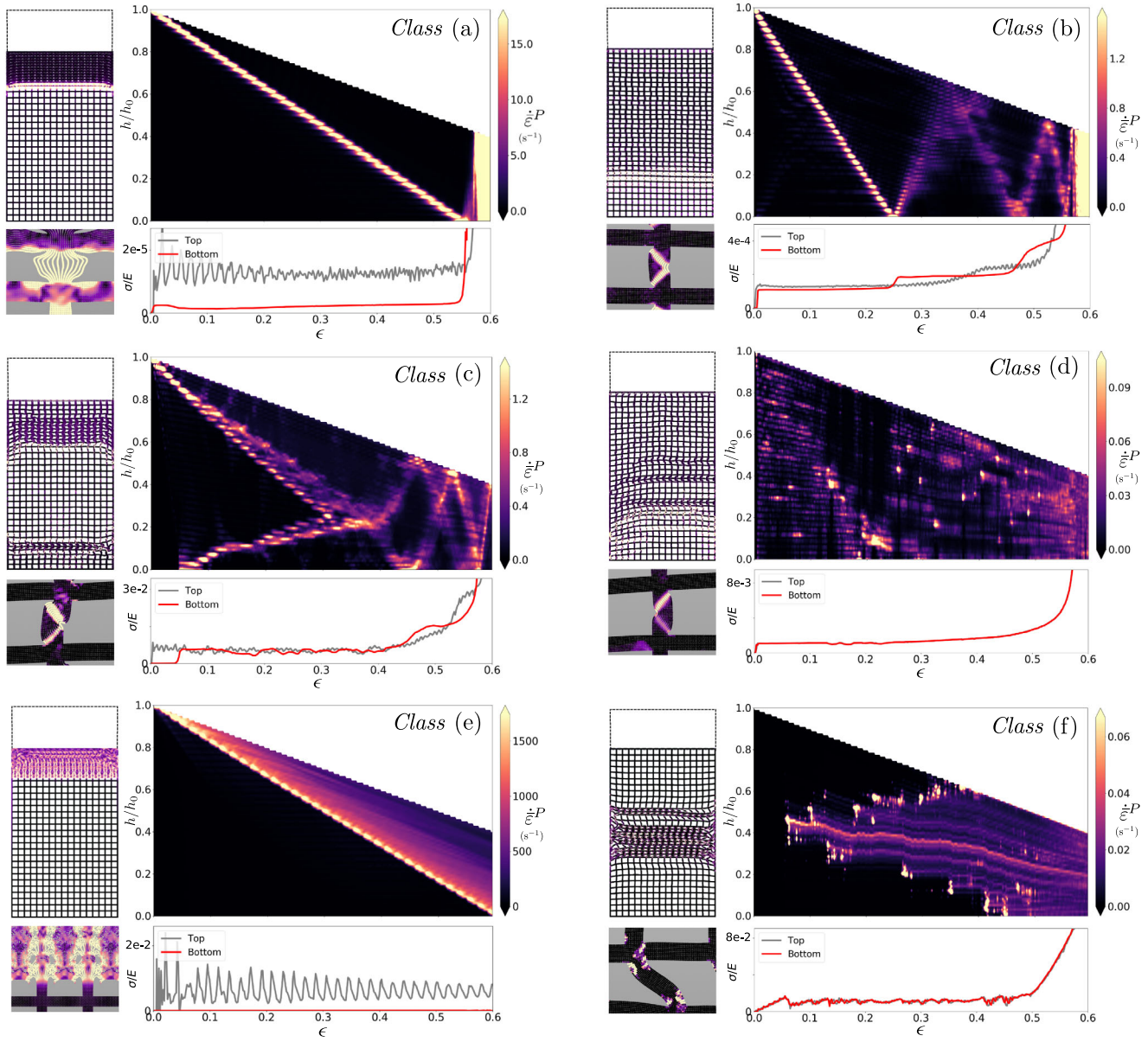

FIG. 1. Typical compaction patterns emanating from a uniaxially loaded confined two-dimensional structured porous media, here with a solid area fraction of $\phi = 0.40$ and the following parameters: (a) $S = 4 \times 10^{-3}$, $R = 10^{-5}$, (b) $S = 4 \times 10^{-3}$, $R = 4 \times 10^{-4}$, (c) $S = 4 \times 10^{-2}$, $R = 2 \times 10^{-2}$, (d) $S = 1.32 \times 10^{-3}$, $R = 4 \times 10^{-3}$, (e) $S = 10^{-1}$, $R = 10^{-5}$, (f) $S = 4 \times 10^{-3}$, $R = 10^{-1}$. Contour plots show the spatiotemporal values of plastic Hencky strain rate $\dot{\bar{\epsilon}}^P = \sqrt{\dot{\boldsymbol{\epsilon}}^P : \dot{\boldsymbol{\epsilon}}^P}$ as the samples are compressed until fully dense from the top under a growing nominally imposed strain $\epsilon = Vt/h_0$. Values on those plots are obtained by averaging over the horizontal direction, neglecting 10% of the area closest to the smooth sidewalls. A snapshot of the structure at $\epsilon = 0.2$ is shown to the left of each case, colored in terms of the local $\dot{\bar{\epsilon}}^P$. An enlarged view is shown below, thus highlighting the state of deformation. Supplemental Movie 1 displays the evolution of the plastic strain rate in the six structures until $\epsilon = 0.6$. The stress σ at the bottom and top plates are plotted below the corresponding contour plots.

continuing to compress the thickened columns. While the band travels through the sample as a moving separation between two regions of different porosities, the stress on the top and bottom plates remains largely constant, as can be seen in the stress-strain curves of Fig. 1(b). However, when a band reflects from a plate, the stress level on it suddenly increases, which can be attributed to increased effective elastic modulus due to the decreasing porosity.

The erratic class (d) also displays column elements that shear under compression, but the location of the columns undergoing plastic deformation is random. Once sheared, these elements thicken a certain amount, and the plastic deformation jumps to a different random location. Because

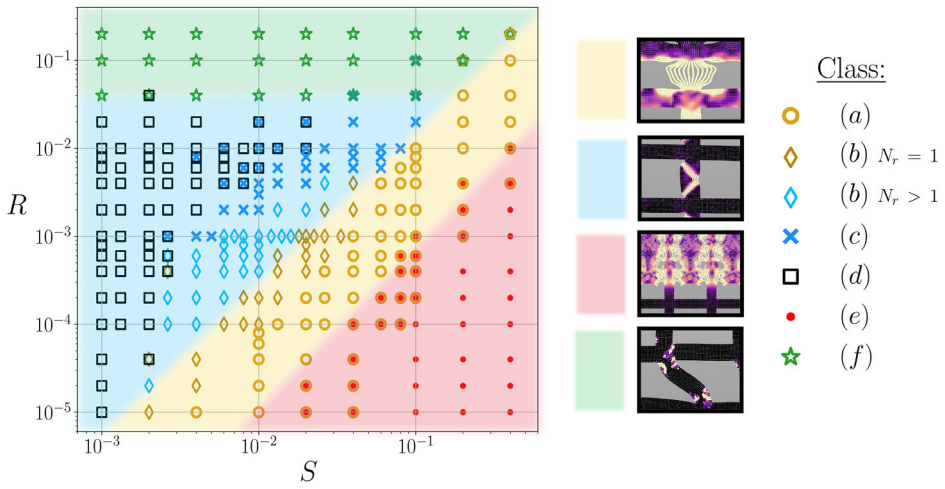

FIG. 2. Compaction patterns classified in the space of S and R for a structure with a solid area fraction $\phi = 0.40$. Note the separation of class (b) based on the number of reflections N_r the compaction band displays. The background colors represent the type of deformation mechanism on the microscale.

of the low imposed plate speed, the stress state remains essentially uniform throughout the structural columns, similar to the situation of the erratic compaction patterns observed in lattice-spring systems [16]. This is in contrast to simulations featuring a (reflecting) compaction band where there is not sufficient time for the elastic stress wave to travel down the sample and equilibrate before the structure yields at the top.

Under low relative strength, R, and high relative imposed plate speed, S, the system develops a class (e) pattern where the upper elements are immediately disturbed and flow into the pores like a plastic fluid, while the lower elements remain elastic, leaving a separating compaction front in between. As seen in Fig. 1(e), the stress exerted on the top plate displays undulations that correspond to the number of voids in the direction of compression. On the other hand, in systems with high strength, class (f), the column elements elastically buckle before plastic deformations occur. From Euler's well-known formula for critical buckling load, we can deduce that the column elements buckle (first mode) before yielding for $R \gtrapprox R_{\mathrm{crit}} = \pi^2 a^2/12$ where a, the aspect ratio of the columns, is determined by the solid fraction ϕ of the structure. If $\phi = 0.40$, then $R_{\mathrm{crit}} \approx 0.05$, consistent with the observations in Fig. 2. With smaller or larger ϕ, the transition to class (f) will occur at lower or higher R_{crit}, respectively.

The speed of a compaction band is related to the number of reflections the band makes and the porosity of the sample. Observing that bands cease to exist at an imposed strain $\epsilon = 1 - \phi$ when the structure has closed all its pores, it follows that the band speed c_b relative to the imposed plate speed V must be given by $c_b/V = (1-\phi)^{-1}$ for nonreflecting bands. For reflecting bands, the ratio c_b/V must be higher, where we let c_b refer to the speed of the band before any reflection has occurred (the speed after reflection is generally comparable or slightly larger than before reflection). Given the solid fraction ϕ_f after the first reflection, we could find a similar expression $c_b/V = (1-\phi/\phi_f)^{-1}$ based on analogous mass conservation calculations as per Olsson [24]. For classes (a) and (b) where a compaction band appears, Fig. 3 shows how the relative band speed increases with the number of reflections. We observe that for reflecting bands c_b/V increases as a power law with the dimensionless parameter $R/S^2 = q_y/(\rho V^2)$, independent of elastic modulus. This dimensionless parameter gives the ratio between the yield stress of the material and the inertia stress, characterizing the resistance of the structure to dynamic impact.

Although only structures with regularly equispaced voids have been treated so far, it is also instructive to consider structures with random void location and size.

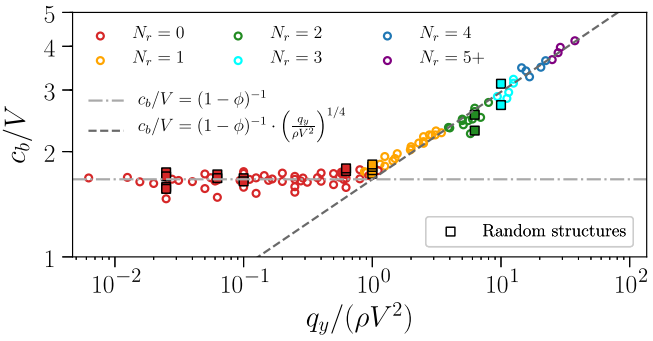

FIG. 3. Speed c_b of the (prereflection) compaction bands, normalized by the imposed compressive speed V, as a function of $q_y/(\rho V^2)$ in log-log scale. The data points are colored according to the number of reflections N_r of the compaction band. Circular and square markers correspond to regular and random structures, respectively.

In this case, the compaction pattern (S, R) classification, as well as the potential band speed, have not been found to deviate significantly from the regular case with identical porosity. Band speeds of such random structures have been included in Fig. 3 for comparison with regular structures. More details are provided in the Supplemental Material [21], which further emphasizes the generality of the results by showing that the dynamic compaction patterns are also not affected by the dimensionality of the problem. In particular, a three-dimensional and a pseudo-one-dimensional structure (i.e., a two-dimensional structure reduced to the smallest horizontal periodic unit) exhibit reflecting compaction bands with the same band speed as the corresponding full two-dimensional structure. In fact, the reduction to a pseudo-one-dimensional structure was exploited to reduce the computational cost associated with the many simulations needed to fully populate Figs. 2 and 3.

The observations presented so far indicate that the general compaction patterns of the porous media are largely independent of the porosity, the particular placement and size of the square pores, the dimensionality of the system, and the material parameters as long as the Mach number S and normalized structural strength R remain constant. The exact combination of these two parameters results in different elastoplastic deformation of the constituent structural elements on the microscale. Notably, the varying ways these microscopic deformation mechanisms lead to pore collapse is correlated to the emergence of propagating bands and their reflection. We highlight that the current model does not rely on any empirical hardening or softening laws, nor any strain rate-dependent effects or parameters. In view of developing a homogenized continuum constitutive model for snow that captures oscillatory compaction bands, Barraclough *et al.* [17] argued that such models must account for the interplay between compression-induced softening and sintering-induced structural healing. In that model, sintering was added as a form of time-dependent hardening to control band reflection (and is undoubtedly an important physical process in snow). While all previous models [16,17,26] consider empirical hardening laws to recover reflecting compaction bands, our observations are in line with Valdes *et al.* [26]—both studies demonstrate that rate-dependent hardening or softening is not necessary for the emergence of such patterns. Although not having explicitly introduced any empirical hardening law, the current model considers the full elastoplastic deformation of the microstructural elements, which, given appropriate values of S and R, will elastoplastically deform (thicken) such that they naturally harden. In the lattice-spring model of Guillard *et al.* [16] where the full elastoplastic deformation of the solid elements is not accounted for (e.g., the springs do not have a spatial extent and the concept of porosity is not well-defined), band reflections were therefore not observed without the addition of a spring hardening law.

In conclusion, this Letter has investigated transient compaction patterns in porous media through numerical experiments. In particular, we have shown that propagating and oscillatory compaction bands can be realized in porous geometries without needing any empirical hardening or strain rate-dependent effects. We argue that the required hardening for band propagation and reflection occurs naturally and has an origin related to the structural deformations leading to universal pore collapse, which can be conceived for any inelastic porous media, including snow and cereals. It was further demonstrated that the manifestation of a given compaction pattern depends on two ratios: one ratio between the yield strength and elastic modulus, and another between the imposed compression speed and the elastic wave speed. This study and its findings are crucial to the understanding and further model development of porous media mechanics, in particular critical phase transitions occurring in geophysical avalanches, earthquakes, and meteorite impacts.

We acknowledge support from the Swiss National Science Foundation (Grant PCEFP2_181227) and the Australian Research Council (Grant DP190103487). We also thank the two anonymous reviewers for their constructive and inspiring comments that contributed to improving the quality of this Letter.

*Corresponding author.
johan.gaume@epfl.ch

[1] J. Heierli, P. Gumbsch, and M. Zaiser, Anticrack nucleation as triggering mechanism for snow slab avalanches, Science **321**, 240 (2008).
[2] J. Gaume, A. van Herwijnen, G. Chambon, N. Wever, and J. Schweizer, Snow fracture in relation to slab avalanche release: Critical state for the onset of crack propagation, Cryosphere **11**, 217 (2017).
[3] H. W. Green, T. E. Young, D. Walker, and C. H. Scholz, Anticrack-associated faulting at very high pressure in natural olivine, Nature (London) **348**, 720 (1990).
[4] L. J. Gibson, M. F. Ashby, G. S. Schajer, and C. I. Robertson, The mechanics of two-dimensional cellular materials, Proc. R. Soc. A **382**, 25 (1982).
[5] S. D. Papka and S. Kyriakides, In-plane crushing of a polycarbonate honeycomb, Int. J. Solids Struct. **35**, 239 (1998).
[6] T. Baxevanis, E. Papamichos, O. Flornes, and I. Larsen, Compaction bands and induced permeability reduction in Tuffeau de Maastricht calcarenite, Acta Geotech. **1**, 123 (2006).
[7] O. Simon and P. Guigon, Correlation between powder-packing properties and roll press compact heterogeneity, Powder Technol. **130**, 257 (2003).
[8] P. N. Mollema and M. A. Antonellini, Compaction bands: A structural analog for anti-mode I cracks in aeolian sandstone, Tectonophysics **267**, 209 (1996).

[9] K. A. Issen and J. W. Rudnicki, Conditions for compaction bands in porous rock, J. Geophys. Res. **105**, 21529 (2000).
[10] P. Baud, E. Klein, and T.-f. Wong, Compaction localization in porous sandstones: Spatial evolution of damage and acoustic emission activity, J. Struct. Geol. **26**, 603 (2004).
[11] U. Kelka, M. Veveakis, D. Koehn, and N. Beaudoin, Zebra rocks: Compaction waves create ore deposits, Sci. Rep. **7**, 14260 (2017).
[12] Y. Abdallah, J. Sulem, and I. Stefanou, Compaction banding in high-porosity carbonate rocks: 2. A gradient-dependent plasticity model, J. Geophys. Res. **125**, e2020JB020610 (2020).
[13] F. Pacheco-Vázquez, T. Omura, and H. Katsuragi, Undulating compression and multistage relaxation in a granular column consisting of dust particles or glass beads, Phys. Rev. Research **3**, 013190 (2021).
[14] V. Vajdova and T.-f. Wong, Incremental propagation of discrete compaction bands: Acoustic emission and microstructural observations on circumferentially notched samples of Bentheim, Geophys. Res. Lett. **30**, 1775 (2003).
[15] J. R. Valdes, F. L. Fernandes, and I. Einav, Periodic propagation of localized compaction in a brittle granular material, Granular Matter **14**, 71 (2012).
[16] F. Guillard, P. Golshan, L. Shen, J. R. Valdes, and I. Einav, Dynamic patterns of compaction in brittle porous media, Nat. Phys. **11**, 835 (2015).
[17] T. W. Barraclough, J. R. Blackford, S. Liebenstein, S. Sandfeld, T. J. Stratford, G. Weinländer, and M. Zaiser, Propagating compaction bands in confined compression of snow, Nat. Phys. **13**, 272 (2017).
[18] D. Sulsky, Z. Chen, and H. L. Schreyer, A particle method for history-dependent materials, Comput. Methods Appl. Mech. Eng. **118**, 179 (1994).
[19] J. Gaume, T. Gast, J. Teran, A. van Herwijnen, and C. Jiang, Dynamic anticrack propagation in snow, Nat. Commun. **9**, 3047 (2018).
[20] L. Blatny, H. Löwe, S. Wang, and J. Gaume, Computational micromechanics of porous brittle solids, Computers and Geotechnics **140**, 104284 (2021).
[21] See Supplemental Material at http://link.aps.org/supplemental/10.1103/PhysRevLett.128.228002 for more information about the numerical scheme as well as random and three-dimensional structures.
[22] C. Park and S. R. Nutt, Anisotropy and strain localization in steel foam, Mater. Sci. Eng. A **299**, 68 (2001).
[23] W. A. Olsson and D. J. Holcomb, Compaction localization in porous rock, Geophys. Res. Lett. **27**, 3537 (2000).
[24] W. A. Olsson, Quasistatic propagation of compaction fronts in porous rock, Mech. Mater. **33**, 659 (2001).
[25] A. Mandal, B. J. Jensen, M. C. Hudspeth, S. Root, R. S. Crum, and M. C. Akin, Direct observations of shock-induced melting in a porous solid using time-resolved x-ray diffraction, Phys. Rev. Mater. **4**, 063604 (2020).
[26] J. R. Valdes, F. Guillard, and I. Einav, Evidence That Strain-Rate Softening Is Not Necessary for Material Instability Patterns, Phys. Rev. Lett. **119**, 118004 (2017).